Engineering properties by long range symmetry propagation initiated at perovskite heterostructure interface

Z. L. Liao[1], R. J. Green[2,4], N. Gauquelin[3], S. Macke[2,5], L. Lin[1], J. Gonnissen[3], R. Sutarto[6], E. P. Houwman[1], Z. Zhong[5], S. Van Aert[3], J. Verbeeck[3], G. A. Sawatzky[2], G. Koster[1*], M. Huijben[1], G. Rijnders[1]

[1]*MESA+ Institute for Nanotechnology, University of Twente, P.O.BOX 217, 7500 AE, Enschede, The Netherlands*

[2]*Quantum Matter Institute and Department of Physics and Astronomy, University of British Columbia, 2355 East Mall , Vancouver, V6T 1Z4, Canada*

[3]*Electron Microscopy for Materials Science (EMAT), University of Antwerp, 2020 Antwerp, Belgium*

[4]*Max Planck Institute for Chemical Physics of Solids, Nöthnitzerstraße 40, 01187 Dresden, Germany*

[5]*Max Planck Institute for Solid State Research, Heisenbergstraße 1, 70569 Stuttgart, Germany*

[6]*Canadian Light Source, Saskatoon, Saskatchewan S7N 2V3, Canada*

Abstract:

In epitaxial thin film systems, the crystal structure and its symmetry deviate from the bulk counterpart due to various mechanisms such as epitaxial strain and interfacial structural coupling, which induce an accompanying change in their properties. In perovskite materials, the crystal symmetry can be described by rotations of 6-fold coordinated transition metal oxygen octahedra, which are found to be altered at interfaces. Here, we unravel how the local oxygen octahedral coupling (OOC) at perovskite heterostructural interfaces initiates a different symmetry in epitaxial films and provide design rules to induce various symmetries in thin films by careful selecting appropriate

* g.koster@utwente.nl

combinations of substrate/buffer/film. Very interestingly we discovered that these combinations lead to symmetry changes throughout the full thickness of the film. Our results provide a deep insight into understanding the origin of induced crystal symmetry in a perovskite heterostructure and an intelligent route to achieve unique functional properties.

Main text:

Diverse electronic phases in solid state materials such as superconductivity, topological insulating phases and ferroelectricity are intimately coupled to crystal symmetry [1-5]. Controlled symmetries have been extensively employed in oxide heterostructures for generating novel properties and functionalities [6-11]. In ABO_3 perovskites, the crystal symmetry resides in the corner sharing oxygen octahedral (BO_6) network [2, 12-14]. These symmetries, or oxygen octahedral rotation (OOR) patterns in perovskite heterostructures, are usually engineered by epitaxial strain [15]. Furthermore, the required connectivity of the octahedra across the heterostructure interface enforces a geometric constraint to the 3-dimensional octahedral network in epitaxial films [16-21]. The control of this oxygen octahedral coupling (OOC) at interfaces has been shown to result in interesting phenomena in ultrathin oxide films [17-21]. However, the effect of the OOC on octahedral tilt angles decays steeply and is found to be confined to layer thicknesses of only 4-8 unit cells (uc) [17-21]. The short range impact of the OOC on the tilt angle was recently further demonstrated for $La_{2/3}Sr_{1/3}MnO_3$ (LSMO)/$NdGaO_3$ (NGO) heterostructure, in which the OOC driven novel anisotropic properties only emerge in LSMO thinner than 8 uc [17]. The limited propagation of the interface-induced

octahedral tilt into the film currently restricts the engineering of perovskite heterostructures with unique functional properties.

The rotational behavior, in-phase or out-of-phase, can still survive even when the magnitude of the octahedral tilt becomes very small. Therefore, the propagation length of the symmetry can be much larger than the propagation of an induced tilt angle. This aspect has been disregarded in the past. Here, we demonstrate and unravel the fundamentally important phenomenon of long range propagation of crystal symmetry induced by OOC in perovskite heterostructures. The symmetry of epitaxial films near interfaces, induced by OOC, propagates deeper throughout the films than the tilt angle itself. This allows us to manipulate electronic and magnetic properties in materials over an extensive thickness range, breaking the current limitation of the normally assumed short range of the impact of OOC.

The symmetry of a perovskite is reflected by the characteristic OOR throughout the crystal, which is usually described using Glazer notation [12]. For example, a Glazer notation $c^+a^-a^-$ corresponds to the orthorhombic Pbnm structure. The Glazer letters hereafter are sequentially corresponding to the rotation about the pseudocubic *a*, *b* and *c*-axes, respectively. For a detailed study of specific OOC effects at interfaces a more precise description of the rotations of each octahedron is required. Therefore, the OOR in a perovskite is patterned into a network of rotation signs of the individual octahedra by defining the clockwise and counterclockwise rotation along specific crystal axes as negative (-) and positive (+) respectively, and no rotation as zero (0), as shown in **Fig. 1a**. The required connectivity of octahedra strictly restricts the adjacent rotation signs, as illustrated by an example of a single tilt system in the right panel of **Fig. 1a**, where

adjacent octahedra residing in a plane normal to the tilt axis require opposite rotation signs about that axis. Further, the in-phase or out-of-phase rotation designations restrict the rotation signs of adjacent octahedra along the tilt axis. Therefore, the rotation behavior of each individual octahedron is fully correlated to that of its neighbor by these two octahedral connectivity rules. For a triple octahedral tilt system, the rotation of each individual octahedron has three components of rotation about three pseudocubic axes and the rotation of an octahedron is characterized by three rotation signs, i.e., (± ± ±), about *a*, *b* and *c*-axis respectively (see **Fig. 1b**). The characteristic Glazer tilt system can be visualized by drawing a rotation signs network of eight octahedra from a unit cell, in which for example a front-bottom-left (FL) octahedron with a specific rotation sign fully determines the whole network. For simplicity, the rotation sign of the front-bottom-left octahedron is used to represent the whole rotation network, e.g., [---] for the bottom rotation signs network in **Fig. 1b(I)**. Disregarding the relative difference in the magnitude of the tilts, the $c^+a^-a^-$ and $a^+a^-a^-$ actually have the same rotation pattern and we will focus on the rotation signs network by simplifying the Glazer notation to $a^+a^-a^-$. There are only two possible rotation networks for $a^+a^-a^-$: the [---] and the [--+] networks, which correspond to different lattice angles α (see Supplementary **Section I**). Taking $CaTiO_3$ (CTO) as an example, the [---] and [--+] networks produce $\alpha < 90^o$ and $\alpha > 90^o$ respectively [22] (see **Fig. 1b(I-II)**).

There are two possible resultant structures when coherently growing an orthorhombic perovskite film (f) on an orthorhombic perovskite $(110)_{orth}$ substrate (s): either $[---]_f/[---]_s$, or $[--+]_f/[---]_s$ (see **Fig. 1b**). The interface of $[---]_f/[---]_s$ naturally maintains an $a^+a^-a^-$ symmetry across the interface, while $[--+]_f/[---]_s$ interface violates the two octahedral

connectivity rules mentioned above (For more detail, see Supplementary **Fig. S1**). To maintain the connectivity of the octahedra, the former is expected to be energetically more favorable, because less octahedral distortion is required to connect the octahedra. Since the symmetry constraints are enforced to every subsequent layer, the symmetry initiated at the interface propagates deeper into the film (see **Fig. 1c**). This analysis is confirmed experimentally in the study of CTO/$NdGaO_3$ (NGO) heterostructures, in which CTO [22] and NGO [23] share the same $c^+a^-a^-$ structure with [---] for $\alpha < 90^o$ and [--+] for $\alpha > 90^o$. The unit cell structure of a 30 uc thick CTO film on NGO $(110)_{orth}$ was determined by X-ray reciprocal space mapping (RSM) of the (0-24), (024), (204), (-204) reflections as shown in **Fig. 1d.** Details of the growth of the films can be found in supplementary **Fig. S2** and **Table S1**. For the orthorhombic $c^+a^-a^-$ structure, the lattice angles β and γ are 90^o and α can be determined as (see Supplementary **Fig. S3**), yielding for our film $\alpha_{CTO} = 89.38^o$. The determined $\alpha_{CTO} < 90^o$ on $\alpha_{NGO} < 90^o$ structure configuration by RSM suggests that the $[---]_f/[---]_s$ interface is energetically more favorable than $[--+]_f/[---]_s$.

Further strong evidence for OOC mediated symmetry propagation is found in the resultant structure of a $SrRuO_3$ (SRO) film on a $DyScO_3$ (DSO) $(110)_{orth}$ substrate. Similar to NGO, the [---] network of DSO corresponds to $\alpha < 90^o$ [24], whereas one has $\alpha > 90^o$ for the [---] network of SRO [25]. The difference in unit cell tilt directions is caused by the different orthorhombic distortions present (see Supplementary **Fig. S4**). Therefore, we still expect a $[---]_f/[---]_s$ growth but with an $\alpha_{SRO} > 90^o$ on $\alpha_{DSO} < 90^o$ structural configuration for SRO/DSO, which is consistent with experimental observation

(see **Fig. 1e**). The RSM of a 30 uc SRO film on DSO shows that α of the SRO film is 90.57^{o}.

In an interface between two perovskites with the same symmetry (homo-symmetric) such as CTO/NGO and SRO/DSO, the OORs can be perfectly matched, hence the resulting OOC effect breaks the mirror symmetry and induces a single domain structure with a single monoclinic tilt direction. In contrast, OORs cannot be matched across an interface between materials with different symmetries (hetero-symmetric), e.g., the interface between rhombohedral ($a^{-}a^{-}a^{-}$) $BiFeO_3$ (BFO) and an orthorhombic ($a^{+}a^{-}a^{-}$) substrate. The BFO has four possible rotation networks: r_4 $[---]_{rhom}$, r_1 $[+--]_{rhom}$, r_2 $[--+]_{rhom}$ and r_3 $[+-+]_{rhom}$ [26, 27] all of which have mismatched rotation signs at an interface with a $[---]_{orth}$ substrate (see **Fig. 2a**). However, different networks have different degrees of mismatch with $[---]_{orth}$. The $[---]_{rhom}$ and $[+--]_{rhom}$ networks have the same degree of mismatch with the $[---]_{orth}$ network in that they both have 2 tilt signs violating the first rule at the interface about the *a*-axis, hence the $[---]_{rhom}$ and $[+--]_{rhom}$ are equally favored for epitaxial growth. The $[--+]_{rhom}$ and $[+-+]_{rhom}$ on $[---]_{orth}$ also have an equal degree of mismatch and thus are equally favored for epitaxial growth, but they have an additional 4 tilt signs violating the second rule about the *c*-axis besides 2 tilt signs violating the first rule about the *a*-axis. Therefore, the $[---]_{rhom}/[---]_{orth}$ and $[+--]_{rhom}/[---]_{orth}$ interfaces with less octahedral mismatch are expected to be energetically more favorable than the $[--+]_{rhom}/[---]_{orth}$ and $[+-+]_{rhom}/[---]_{orth}$ interfaces during growth. Experimentally, the r_4 ($[---]_{rhom}$) and r_1 ($[+--]_{rhom}$) domains indeed are found to be energetically more favorable when BFO films are grown on orthorhombic $REScO_3$ (RSO) (RE= Dy, Gd, Tb) and SRO $(110)_{orth}$ substrates [27-29] (see **Fig. 2b**). The different structure configurations of $\alpha_{BFO} < 90^{o}$ on

$\alpha_{RSO} < 90^o$ vs $\alpha_{BFO} < 90^o$ on $\alpha_{SRO} > 90^o$ are due to the fact that the RSO and SRO possess $\alpha < 90^o$ and $\alpha > 90^o$ respectively for the same $[---]_{orth}$ network. In conclusion, the domain structures of BFO on different orthorhombic substrates are uniformly explained by the OOC mediated symmetry propagation considerations presented above.

If the OOC effect at a hetero-symmetric interface is strong enough to induce a different OOR pattern in a film near the interface to match the substrate OOR, the initiated different symmetry can propagate deeply throughout the film. An example is the structure of a $La_{2/3}Sr_{1/3}MnO_3$ (LSMO) film on an NGO $(110)_{orth}$ substrate. The bulk LSMO is rhombohedral ($a^-a^-a^-$), but the OOC effect at the LSMO/NGO interface is so strong that one out-of-phase rotation about the *a*-axis in LSMO near the interface (within ~ 3 uc) is converted into in-phase ($a^- \rightarrow a^+$) [17]. As a result, the near interface LSMO becomes orthorhombic. Although the effect of OOC on the magnitude of the octahedral tilt decays steeply [17], the characteristic orthorhombic structure still survives over an extensive thickness range, resulting in an orthorhombic structure in thick LSMO films. The RSM of a 30 uc LSMO film shows that the LSMO film possesses an orthorhombic structure with $a^+b^-c^-$ Glazer notation ($P2_1/m$) [15] (see **Fig. 3a**). The observed $\alpha_{LSMO} > 90^o$ on $\alpha_{NGO} < 90^o$ configuration indicates that the $[---]_{orth}$ network of LSMO corresponds to $\alpha > 90^o$. The $\alpha_{LSMO} > 90^o$ on $\alpha_{NGO} < 90^o$ configuration growth is further microscopically revealed by the scanning transmission electron microscopy (STEM). STEM high angle annular dark field (HAADF) cross-section image shows that the unit cell of LSMO is relatively tilted with respect to the NGO unit cell (see **Fig. 3b**). The relative tilt angle (defined by $\Delta\alpha$ as shown in the inset of **Fig. 3b**) is estimated from the B-site positions which are determined using statistical parameter estimation theory [30] (Supplementary **Fig. S5**). As shown in

the plot of B site (X, Y) positions in **Fig. 3c**, a sudden change of the slope occurs at the interface which cannot be due to image drift and is therefore ascribed to different monoclinic tilt angles in LSMO and NGO. A relative tilt of $\Delta\alpha=\tan^{-1}(k_{LSMO})-\tan^{-1}(k_{NGO})\approx 0.96\pm 0.06^{o}$ obtained from the STEM image, which agrees well the value of 1^{o} extracted from RSM (See **Fig. 3a** and Supplementary **Table S2**).

The strong impact of the OOC on the symmetry of perovskite heterostructures is further observed when engineering the symmetries through an additional buffer layer. By growing a $SrTiO_3$ (STO) film, which does not have tilt in its bulk form, on a NGO $(110)_{orth}$ substrate, one obtains a STO buffer layer exhibiting a new symmetry of $a^0a^0c^-$ with $\alpha = 90^{o}$ (For details, see Supplementary **Fig. S6**). The LSMO film on this STO buffer layer exhibits a different symmetry from the non-buffered LSMO. According to the RSM of the (024) and (0-24) reflections of the buffered LSMO (see **Fig. 3d**), (the data of (204) and (-204) for all films mentioned are always symmetric and not shown here), the α of buffered LSMO becomes 90^{o}, indicating an $a^0b^+c^-$ (Cmcm) structure. The change of structure due to the STO buffer layer is also atomically visualized in STEM image shown in **Fig. 3e**, where no relative unit cell tilt exists between LSMO and STO, although it is present at the STO/NGO interface. The relative tilt angle can be calculated using the B-site (X,Y) positions as shown in **Fig. 3f**. A sudden change of the slope is observed when crossing the STO/NGO interface, due to the tetragonal structure of the STO on the orthorhombic NGO, but is absent at the LSMO/STO interface. The relative tilt angle $\Delta\alpha$ between LSMO/STO and NGO is about 0.76 ± 0.06^{o}, in good agreement with the number obtained from RSM (see Supplementary **Table S2**). Thus, the mirror symmetry recovered in the STO layer is now transferred into the LSMO layer.

If only considering the strain effect, the LSMO can accommodate the in-plane strain induced by NGO via shaping its structure into either $a^0b^+c^-$ or $a^+b^-c^-$, which both can produce a < b and $\gamma = 90^o$ lattice parameters. Since the buffered and non-buffered LSMO share the same strain (see **Fig. 3a and 3d**), the observed different symmetries of buffered and non-buffered LSMO films on NGO further supports the central role of the OOC mediated symmetry propagation effect in determining the structure of perovskite heterostructures. A similar effect is observed in $NdNiO_3$ (NNO)/STO/NGO $(110)_{orth}$ (see **Fig. 4a**) and SRO/STO/DSO $(110)_{orth}$ (see Supplementary **Fig. S6**). With an additional STO buffer layer, the orthorhombic NNO and SRO are switched to tetragonal structures. (see Supplementary **Table S2**). Even in some materials where the intrinsic chemical pressure dominates over epitaxial growth in determining their crystal symmetry, the interfacial OOC effect can still affect the domain structure, e.g., BFO/$REScO_3$ as discussed above and CTO/STO/NGO [see Supplementary **Fig. S6**].

The OOC is usually considered as an effect to modify the octahedral tilt angle in a very short range of 4-8 uc, however, its long range impact on symmetry has a much more profound impact on the properties of a film. **Figure 4b** shows the XRD results of 30 uc $NdNiO_3$ (NNO) films on NGO $(110)_{orth}$ substrates without (NN) and with (NSN) a 6 uc STO buffer layer. The shift in the NNO (002) peak position for NSN as compared to that for NN indicates a larger out-of-plane lattice constant. As a consequence, the metal to insulator transition (MIT) and conductivity of the films are quite different as can be seen in **Fig. 4c**. The MIT temperature (T_{MIT}) in non-buffered NNO is ~ 182 K, similar to previously reported values in bulk and films [31-33], but with a STO buffer layer, the T_{MIT} is significantly lowered down to ~149 K. At low temperatures (T < 150 K), the

resistivity of the buffered NNO is almost two orders of magnitude less that of non-buffered NNO (see **Fig. 4c**).

To investigate the impact of this change of symmetry on the electronic and magnetic structure of the NNO films, we performed X-ray absorption spectroscopy (XAS) and resonant magnetic diffraction (RMD) measurements [34]. **Figure 5a** shows the temperature-dependent Ni L_3-edge XAS of the NSN and NN samples. The main features of the XAS—two primary peaks at low temperatures in the insulating regime, which merge together at higher temperatures in the metallic regime—are consistent with previous reports on bulk nickelates [35]. However, the fine details of the two samples are distinctly different. For the STO-buffered film, the two primary peaks are closer together, which is comparatively similar to $PrNiO_3$ (PNO) in the bulk phase diagram [35]. This is consistent with the reduced OOR due to the symmetry imposed by the STO layer. By going from bulk NNO to PNO in the nickelate phase diagram, octahedral rotations are also reduced and the T_{MIT} shifts to lower temperatures [35], as observed in our symmetry-engineered films.

Figure 5a also shows the energy dependence of the RMD signal at the Ni L_3 resonance. The signal arises from the (1/4,1/4,1/4) magnetic Bragg reflection, indicative of the E'-type antiferromagnetic ordering of the nickelates. For both films, we find a robust diffraction signal at 22 K, with an energy dependence similar to what has been measured for other nickelates [36,37]. In **Fig. 5b**, we show the temperature dependence of the RMD signal, with the X-ray energy tuned to that of the L_3 resonance maximum. Similar to what was observed for the MIT, we find that the symmetry change imposed by the STO buffer layer reduces the Néel temperature (T_N) of the NNO film from 180 K down to ~150 K.

Oxygen K-edge XAS, shown in **Fig. 5c**, provides a measurement of the Ni-O covalency in the films. The strong pre-peak near 528.5 eV originates from excitations into strongly hybridized Ni 3d – O 2p unoccupied states just above the Fermi level. For the buffered NNO, the pre-peak is wider (FWHM of 1.2 eV versus 1.1 eV as indicated by the arrows for each case) and is pushed to a slightly higher energy, both consistent with a wider bandwidth due to the reduction in OOR for the buffered film. A spectrum from a pure $SrTiO_3$ crystal is shown as well, verifying that a signal from the STO buffer layer does not contribute to the pre-peak region and only adds a small bump at higher energies. The observed increase of the bandwidth due to the STO buffer layer is possibly the driving force [31,35,38] for enhanced conductivity and reduced Néel temperature in the buffered NNO film. Although the exact mechanism for the MIT in NNO films is complex and still a matter of debate [31-39], our finding of the impact of symmetry on T_{MIT} and T_N suggests that the OOR which controls the electron bandwidth could play a vital role [31]. Therefore, the symmetry change imposed by the $SrTiO_3$ buffer layer moves the NNO film significantly across the nickelate phase diagram—as evidenced by the resistivity, magnetism, and general electronic structure—providing a unique and new way of tuning the macroscopic properties.

The control of properties by the engineering of symmetry propagation is found also in LSMO films (For details, see Supplementary **Fig. S7**). A 6 uc STO buffered 30 uc LSMO film is much more conductive and has higher Curie temperature than a non-buffered LSMO film. Previously reported substrate symmetry effects involving materials such as LSMO [20] or NNO [33] were achieved by using different substrates of NGO $(001)_{orth}$, NGO $(110)_{orth}$, or LSAT (001), where a small difference in lattice mismatch always exists,

hence the effect of strain cannot be fully ruled out. As there is no modification of the strain but solely an engineering of the symmetry of the film, our results unambiguously reveal the strong impact of long range symmetry propagation on properties and functionalities. This long range variation of symmetry enforced by an ultrathin buffer layer also indicates the capability to tailor structure and their properties at unit cell thickness level. Since the octahedral rotation can also cause an octahedral distortion [14], in addition to a change of the octahedral tilt, such control of the symmetry can be used for engineering of magnetic anisotropy [40], orbital ordering [41], ferroelectricity [42] and magnetism [43].

In conclusion, we have illustrated a strong interfacial OOC mediated long range symmetry propagation effect at perovskite oxide interfaces. The symmetry propagation enables us to engineer the symmetry of oxide heterostructures in a flexible way by using either homo-symmetric or hetero-symmetric interfaces. The interfacial OOC initiates symmetry propagating over extensive distances and subsequently allows us to tune the symmetries of epitaxial films by locally varying the substrate symmetry via the insertion of an ultrathin buffer layer. The octahedral network is common in all perovskite heterostructures, hence our findings provide a deep insight into understanding structure-properties relation in perovskite heterostructures and superlattices. The OOC mediated long range symmetry propagation also provides us with a new strategy to engineer structure and functionalities in oxide heterostructure over distances comparable of that of the strain.

Methods:

The perovskite oxide films were grown by pulsed layer deposition (PLD) on single terminated $NdGaO_3$ $(110)_{orth}$ (NGO) and $DyScO_3$ $(110)_{orth}$ (DSO) substrates. The single terminated NGO and DSO surfaces were obtained by a combined chemical etching and subsequent high temperature annealing (More details can be found in the Supplementary Information). Reflection high energy electron diffraction (RHEED) was used to accurately control the individual layer thicknesses. Transport properties were characterized by Quantum Design Physics Property Measurement System (QD-PPMS). The lattice structures of the thin films were determined by PANalytical-X'Pert materials research diffractometer (MRD) at high resolution mode. Atomic scale characterization of the lattice structure was performed by Cs-corrected scanning transmission electron microscopy (STEM) on the X-Ant-Em instrument at the University of Antwerp. Cross-sectional cuts of the samples along the NGO $[1\text{-}10]_{orth}$ direction were prepared using a FEI Helios 650 dual-beam Focused Ion Beam device.

The X-ray absorption spectroscopy (XAS) and resonant magnetic diffraction (RMD) were performed using an in-vacuum 4-circle diffractometer at the Resonant Elastic and Inelastic X-ray Scattering (REIXS) beamline at Canadian Light Source (CLS) in Saskatoon, Canada. The beamline has a flux of 5×10^{12} photon/s and photon energy resolution of 10^{-4} eV. The base pressure of the diffractometer chamber was kept lower than 10^{-9} Torr. The XAS spectra were measured using the total fluorescence yield method, with the incident photons at an angle of 30 degrees from the surface. At the Ni L_3 edge, π-polarized photons were used (polarization vector within the sample a-c pseudocubic

plane), while at the oxygen K edge, measurements with π and σ polarizations were averaged.

References:

[1] Anderson, P.W., Basic Notions of Condensed Matter Physics (Westview Press, Boulder, CO) (1997).

[2] Gopalan, V. & Litvin, D.B., Rotation-Reversal Symmetries in Crystals and Handed Structures, *Nat. Mater.* **10**, 376 (2011).

[3] Tsuei, C.C. & Kirtley, J.R., Pairing Symmetry in Cuprate Superconductors, *Rev. of Modern Phys.* **72**, 969 (2000).

[4] Qi, X.L. & Zhang, S.C., Topological Insulators and Superconductors, *Rev. of Modern Phys*. **83**, 1057 (2011).

[5] Schelkens, R., Ferroelectric and Antiferroelectric Symmetry Groups*, Physica Status Solidi (b)* **37**, 739 (1970).

[6] Disa, A.S., Kumah, D.P., Malashevich, A., Chen, H.H., Arena, D.A., Specht, E.D., Ismail-Beigi, S., Walker, F.J. & Ahn, C.H., Orbital Engineering in Symmetry-Breaking Polar Heterostructures, *Phys. Rev. Lett.* **114**, 026801 (2015)

[7] Warusawithana, M.P., Colla, E.V., Eckstein, J.N. & Weissman, M.B., Artificial Dielectric Superlattices with Broken Inversion Symmetry, *Phys. Rev. Lett.* **90**, 036802(2003).

[8] Lee, H.N., Christen, H.M., Chisholm, M.F., Rouleau, C.M. & Lowndes, D.H., Strong Polarization Enhancement in Asymmetric Three-Component Ferroelectric Superlattices, *Nature* **433**, 395 (2005).

[9] Wang, J., Neaton, J.B., Zheng, H., Nagarajan, V., Ogale, S.B., Liu, B., Viehland, D., Vaithyanathan, V., Schlom, D.G., Waghmare, U.V., Spaldin, N.A., Rabe, K.M., Wuttig, M. & Ramesh, R., Epitaxial $BiFeO_3$ Multiferroic Thin Film Heterostructures, *Science* **299**, 1719 (2003).

[10] Boschker, H., Kautz, J., Houwman, E.P., Siemons, W., Blank, D. H. A., Huijben, M., Koster, G., Vailionis, A. & Rijnders, G., High-Temperature Magnetic Insulating Phase in Ultrathin $La_{0.67}Sr_{0.33}MnO_3$ Films, *Phys. Rev. Lett.* **109**, 157207 (2012).

[11] Ward, T.Z., Budai, J.D., Gai, Z., Tischler, J.Z., Yin, L. & Shen, J., Elastically Driven Anisotropic Percolation in Electronic Phase-Separated Manganites, *Nature Phys*. **5**, 885 (2009).

[12] Glazer, A.M., Classification of Tilted Octahedral in Perovskites, *Acta Cryst.* **B28**, 3384 (1972).

[13] Howard, C.J. & Stokes, H.T., Group-Theoretical Analysis of Octahedral Tilting in Perovskites, *Acta Cryst.* **B54**, 782 (1998).

[14] Woodward, P.M., Octahedral Tilting in Perovskites. I. Geometrical Considerations, *Acta Cryst*. **B53**, 32 (1997).

[15] Vailionis, A., Boschker, H., Siemons, W., Houwman, E.P., Blank, D.H.A., Rijnders, G. & Koster, G., Misfit Strain Accommodation in Epitaxial ABO_3 Perovskites: Lattice Rotations and Lattice Modulations, *Phys. Rev. B* **83 (6),** 064101(2011).

[16] Rondinelli, J.M., May, S.J. & Freeland, J.W., Control of Octahedral Connectivity in Perovskite Oxide Heterostructures: An Emerging Route to Multifunctional Materials Discovery, *MRS Bull.* **37**, 261 (2012).

[17] Liao, Z., Huijben, M., Zhong, Z., Gauquelin, N., Macke, S., Green, R.J., Aert, S.V, Verbeeck, J., Tendeloo, G.V., Held, K., Sawatzky, G.A., Koster, G. & Rijnders, G., Controlled Lateral Anisotropy in Correlated Manganite Heterostructures by Interface-Engineered Oxygen Octahedral Coupling, *Nature Mater*. (2016), doi:10.1038/nmat4579.

[18] Kan, D., Aso, R., Sato, R., Mitsutaka Haruta, M., Kurata, H. &Shimakawa, Y.Tuning magnetic anisotropy by interfacially engineering the oxygen coordination environment in a transition metal oxide, *Nature Materials* (2016), doi:10.1038/nmat4580.

[19] He, J., Borisevich, A.Y., Kalinin, S. V., Pennycook, S.J. & Pantelides, S.T., Control of Octahedral Tilts and Magnetic Properties of Perovskite Oxide Heterostructures by Substrate Symmetry, *Phys. Rev. Lett.* **105**, 227203 (2010).

[20] Moon, E.J., Balachandran, P.V., Kirby, B.J., Keavney, D.J., Sichel-Tissot, R.J., Schlepütz, C.M., Karapetrova, E., Cheng, X.M., Rondinelli, J.M. & May, S.J., Effect of Interfacial Octahedral Behavior in Ultrathin Manganite Films, *Nano Lett.* **14(5),** 2509 (2014).

[21] Moon, E.J., Colby, R., Wang, Q., Karapetrova, E., Schlepütz, C.M., Fitzsimmons, M.R. & May, S.J., Spatial Control of Functional Properties via Octahedral Modulations in Complex Oxide Superlattices, *Nat. Commun.* **5**, 5710 (2014).

[22] Beran, A., Libowitzky, E. & Armbruster, T., A Single-crystal Infrared Spectroscopic and X-ray Diffraction Study of Untwinned San Benito Perovskite, *Can Mineral* **34**, 803 (1996).

[23] Vasylechko, L., Akselrud, L., Morgenroth, W., Bismayer, U., Matkovskii, A. & Savytskii, D., The Crystal Structure of $NdGaO_3$ at 100 K and 293 K Based on Synchrotron Data, *J. Alloys Compd.* **297**, 46 (2000).

[24] Velickov, B., Kahlenberg, V., Bertram, R. & Bernhagen, M., Crystal Chemistry of $GdScO_3$, $DyScO_3$, $SmScO_3$ and $NdScO_3$, *Z. Kristallogr*. **222**, 466 (2007).

[25] Gardner, J.S., Balakrishnan, G. & Paul, D.McK., Neutron Powder Diffraction Studies of Sr_2RuO_4 and $SrRuO_3$, *Physica C* **252**, 303 (1995).

[26] Ito, T., Ushiyama, T., Yanagisawa, Y., Kumai, R. & Tomioka, Y., Growth of Highly Insulating Bulk Single Crystals of Multiferroic $BiFeO_3$ and Their Inherent Internal Strains in the Domain-Switching Process, *Cryst. Growth Des*. **11**, 5139 (2011).

[27] Johann, F., Morelli, A., Biggemann, D., Arredondo, M. & Vrejoiu, I., Epitaxial Strain and Electric Boundary Condition Effects on the Structural and Ferroelectric Properties of $BiFeO_3$ Films, *Phys. Rev. B* **84**, 094105 (2011).

[28] Folkman, C.M., Baek, S.H., Jang, H.W., Eom, C.B., Nelson, C.T., Pan, X.Q., Li, Y.L., Chen, L.Q., Kumar, A., Gopalan, V. & Streiffer, S.K., Stripe Domain Structure in Epitaxial (001) $BiFeO_3$ Thin Films on Orthorhombic $TbScO_3$ Substrate, *Appl. Phys. Lett.* **94**, 251911 (2009).

[29] Chen, Z.H., Damodaran, A.R., Xu, R., Lee, S. & Martin, L.W., Effect of "Symmetry Mismatch" on the Domain Structure of Rhombohedral $BiFeO_3$ Thin Films, *App. Phys. Lett.* **104**, 182908 (2014).

[30] den Dekker, A.J., Gonnissen, J., De Backer, A., Sijbers, J. and Van Aert, S., Estimation of unknown structure parameters from high-resolution (S)TEM images: What are the limits?, *Ultramicroscopy* 134, 34 (2013).

[31] Zhou, J.-S., Goodenough, J.B. & Dabrowski, B., Exchange Interaction in the Insulating Phase of $RNiO_3$, *Phys. Rev. Lett.* **95**, 127204 (2005).

[32] Scherwitzl, R., Zubko, P., Lezama, I.G., Ono, S., Morpurgo, A.F., Catalan, G. & Triscone J.M., Electric-Field Control of the Metal-Insulator Transition in Ultrathin $NdNiO_3$ Films, *Adv. Mater.* **22**, 5517 (2010).

[33] Lian, X.K., Chen, F., Tan, X., Chen, P., Wang, L., Gao, G.Y., Jin, S.W. & Wu, W.B., Anisotropic-Strain-Controlled Metal-Insulator Transition In Epitaxial $NdNiO_3$ Films Grown on Orthorhombic $NdGaO_3$ Substrates, *Appl. Phys. Lett.* **103**, 172110 (2013).

[34] Hawthorn, D.G., He, F., Venema, L., Davis, H., Achkar, A.J., Zhang, J., Sutarto, R., Wadati, H., Radi, A., Wilson, T., Wright, G., Shen, K.M., Geck, J., Zhang, H., Novák, V. & Sawatzky, G.A., An In-vacuum Diffractometer for Resonant Elastic Soft X-ray Scattering, *Rev. Sci. Instrum*. **82**, 073104 (2011).

[35] Freeland, J.W., Veenendaal, M.V. & Chakhalian, J., Evolution of Electronic Structure Across the Rare-Earth $RNiO_3$ Series, arXiv: 1504.02802.

[36] Frano, A., Schierle, E., Haverkort, M.W., Lu, Y., Wu, M., Blanco-Canosa, S., Nwankwo, U., Boris, A.V., Wochner, P., Cristiani, G., Habermeier, H.U., Logvenov, G., Hinkov, V., Benckiser, E., Weschke, E. & Keimer, B., Orbital Control of Noncollinear Magnetic Order in Nickel Oxide Heterostructures, *Phys. Rev. Lett.* **111**, 106804 (2013).

[37] Scagnoli, V., Staub, U., Mulders, A.M., Janousch, M., Meijer, G.I., Hammerl, G., Tonnerre, J.M. & Stojic, N., Role of Magnetic and Orbital Ordering at the Metal-Insulator Transition of $NdNiO_3$, *Phys. Rev. B* **73,** 100409(R) (2006).

[38] Liu, J., Kargarian, M., Kareev, M., Gray, B., Ryan, P.J., Cruz, A., Tahir, N., Chuang, Y.D., Guo, J.H., Rondinelli, J.M., Freeland, J.W., Fiete, G.A. & Chakhalian, J., Heterointerface Engineered Electronic and Magnetic Phases of $NdNiO_3$ Thin Films, *Nat. Commun.* **4**, 2714 (2013).

[39] Liu, J., Kareev, M., Meyers, D., Gray, B., Ryan, P., Freeland, J.W. & Chakhalian, J., Metal-Insulator Transition and Orbital Reconstruction in Mott-Type Quantum Wells Made of $NdNiO_3$, *Phys. Rev. Lett.* **109**, 107402 (2012).

[40] Boschker, H., Mathews, M., Houwman, E.P., Nishikawa, H., Vailionis, A., Koster, G., Rijnders, G. & Blank, D.H.A., Strong Uniaxial In-plane Magnetic Anisotropy of (001)-and (011)-Oriented $La_{0.67}Sr_{0.33}MnO_3$ Thin Films on $NdGaO_3$ Substrates, *Phys. Rev. B* **79**, 214425 (2009).

[41] Mizokawa, T., Khomskii, D.I. & Sawatzky, G.A., Interplay Between Orbital Ordering and Lattice Distortions in $LaMnO_3$, YVO_3, and $YTiO_3$, *Phys. Rev. B* **60**, 7309 (1999).

[42] Benedek N.A. & Fennie, C.J., Hybrid Improper Ferroelectricity: A Mechanism for Controllable Polarization-Magnetization Coupling, *Phys. Rev. Lett.* **106**, 107204 (2011).

[43] Ganguli, N. & Kelly, P.J., Tuning Ferromagnetism at Interfaces between Insulating Perovskite Oxides, *Phys. Rev. Lett.* **113**, 127201 (2014).

Acknowledgements:

We thank B. Keimer for valuable discussions. M.H., G.K. and G.R. acknowledge funding from DESCO program of the Dutch Foundation for Fundamental Research on Matter (FOM) with financial support from the Netherlands Organization for Scientific Research (NWO). This work was funded by the European Union Council under the 7th Framework Program (FP7) grant nr NMP3-LA-2010-246102 IFOX. J.V. and S.V.A. acknowledge financial support from the Research Foundation Flanders (FWO, Belgium) through project fundings (G.0044.13N, G.0374.13N, G.0368.15N, G.0369.15N). The Qu-Ant-EM microscope was partly funded by the Hercules fund from the Flemish Government. N.G. acknowledges funding from the European Research Council under the 7th Framework Program (FP7), ERC Starting Grant 278510 VORTEX. N.G., J.G., S.V.A., J.V. acknowledge financial support from the European Union under the Seventh Framework Program under a contract for an Integrated Infrastructure Initiative (Reference No. 312483-ESTEEM2). The Canadian work was supported by NSERC and the Max Planck-UBC Centre for Quantum Materials. Some experiments for this work were performed at the Canadian Light Source, which is funded by the Canada Foundation for Innovation, NSERC, the National Research Council of Canada, the Canadian Institutes of Health Research, the Government of Saskatchewan, Western Economic Diversification Canada, and the University of Saskatchewan.

Author Contributions:

Z.L. concept design, film growth and magnetic/transport measurements. Data analysis and interpretation: Z.L., R.J.G., E.H., M.H., G.K., G.R.; PLD, AFM and XRD: Z.L, L.L; STEM measurements and analysis: N.G., J.G, S.V.A., J.V.; XAS and RMD measurements and analysis: R.J.G, S.M., R.S, Z.L, G.A.S.; All authors extensively discussed the results and were involved in the writing of the manuscript.

Additional information

Supplementary information is available in the online version of the paper. Reprints and permissions information is available online at www.nature.com/reprints. Correspondence and requests for materials should be addressed to G.K.

Competing financial interest

The authors declare no competing financial interests.

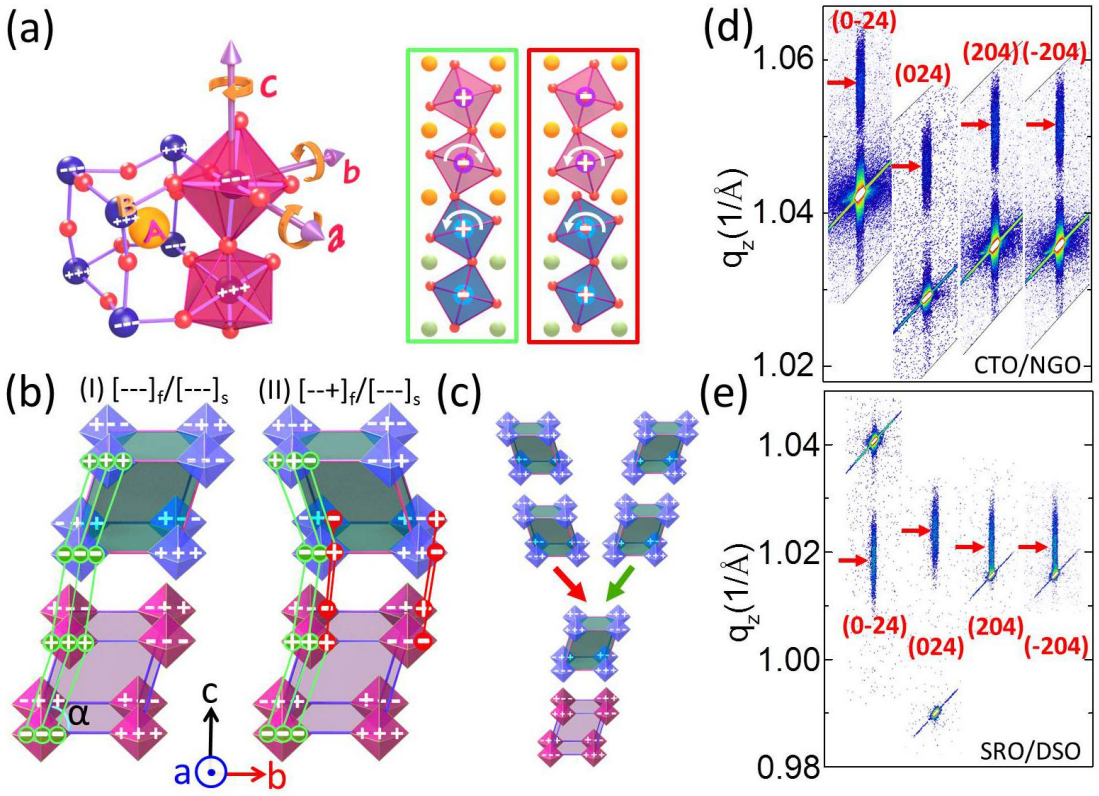

Figure 1: Symmetry propagation initiated at interface. (a) Left, the definition of the rotation sign of an individual octahedron in an ABO_3 perovskite unit cell with clockwise (+) and anti-clockwise (-); Right, connectivity of octahedra for different rotation sign patterns in a single tilt system. The letters A and B indicate the A-site and B-site atoms respectively. (b) Rotation signs network across CTO/NGO interface. (I) and (II) show the $[---]_f/[---]_s$ and $[--+]_f/[---]_s$ configurations respectively. The green "⟜⟜" highlight some of the matched tilt signs while all the unmatched tilt signs are highlighted by red "⟜⟜". (c) The symmetry constraint shown in (b) is

enforced to every subsequent layer. Green and red arrows indicate the preferred and un-preferred growth respectively. RSM of (0-24), (024), (204) and (-204) reflections for (d) 30 uc CTO/NGO and (e) 30 uc SRO/DSO. The film peaks are indicated by arrows and the brightest peaks come from substrate.

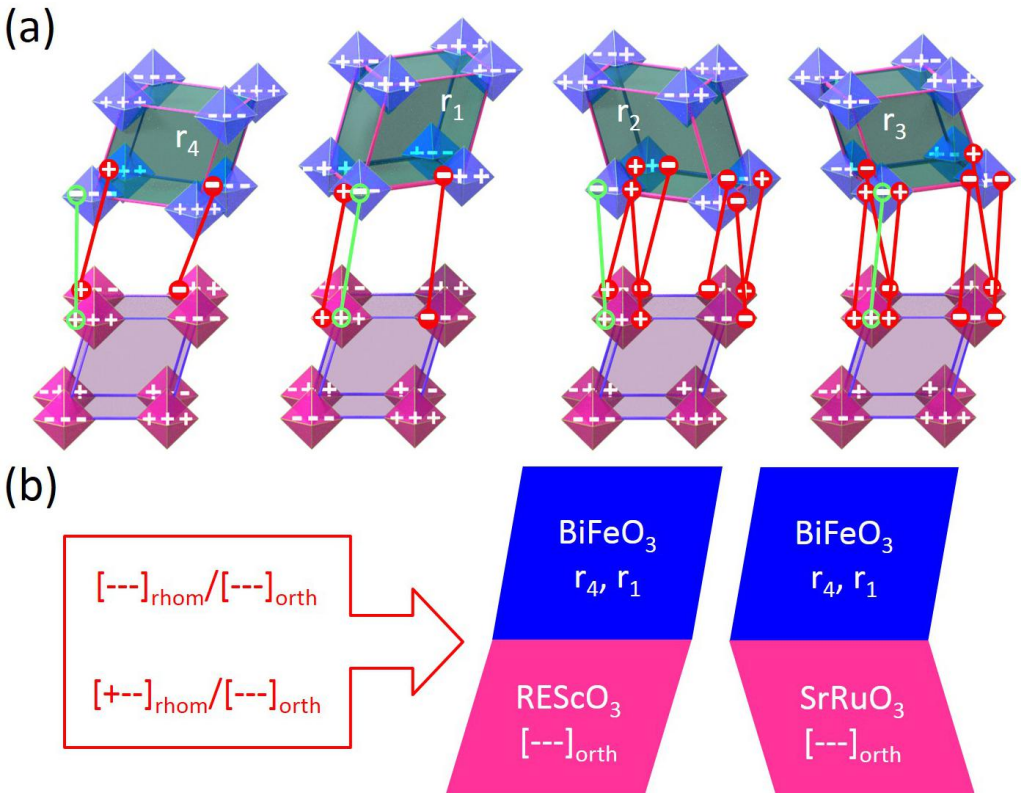

Figure 2: Interfacial OOC induced domain structure of rhombohedral ($a^-a^-a^-$) $BiFeO_3$ film on orthorhombic $(110)_{orth}$ substrate. (a) Octahedral rotation signs network at the interface of $BiFeO_3$ and an orthorhombic $(110)_{orth}$ substrate. The $a^-a^-a^-$ Glazer tilt system has four different rotation networks $[---]_{rhom}$, $[+--]_{rhom}$, $[--+]_{rhom}$ and $[+-+]_{rhom}$. The green "o–o" highlight some of the matched tilt signs while all the unmatched tilt signs across interface are highlighted by red "o–o".

(b) Domain structures of $BiFeO_3$ films on orthorhombic $REScO_3$ and $SrRuO_3$ $(110)_{orth}$ substrates. Structures adapted from ref. [27-29].

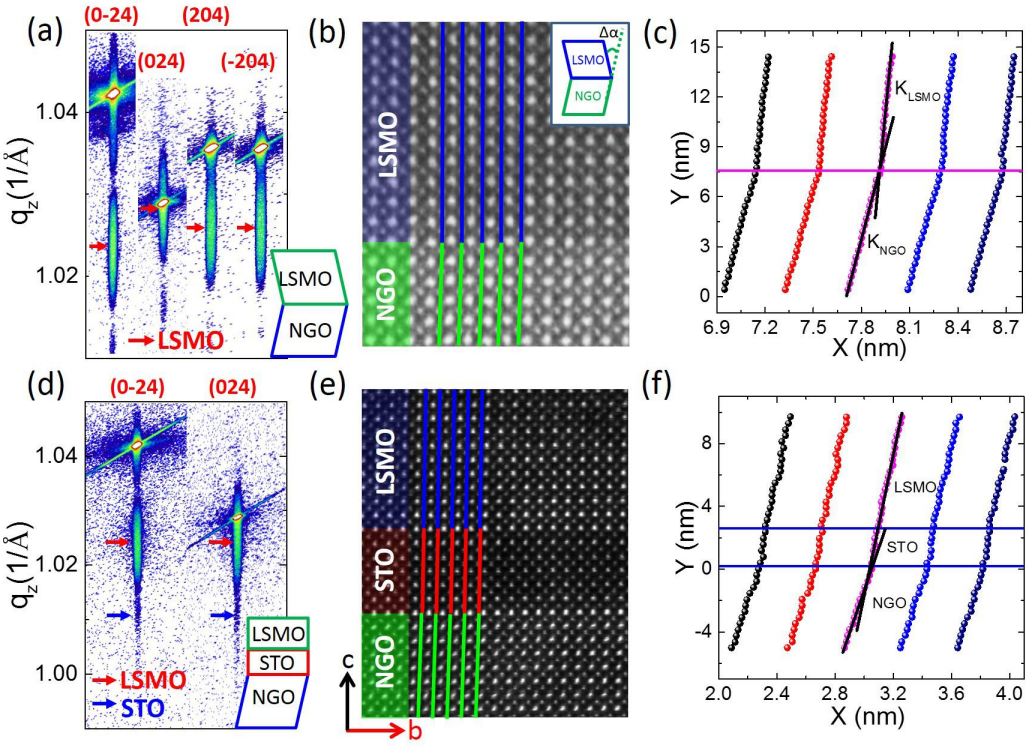

Figure 3: Tailoring structure by interface symmetry engineering. RSM of LSMO films (a) with and (d) without 6 uc STO buffer layers. HAADF cross-section image of 30 uc LSMO films (b) with and (e) without 6 uc STO buffer layers. Inset image at top-right corner of (b) indicates the definition of relative unit cell tilt angle Δα. (c) The positions (X, Y) of B site atoms from five columns marked by lines in (b). K represents the slope of the curve. (f) The positions (X, Y) of B site atoms from five columns marked by lines in (e).

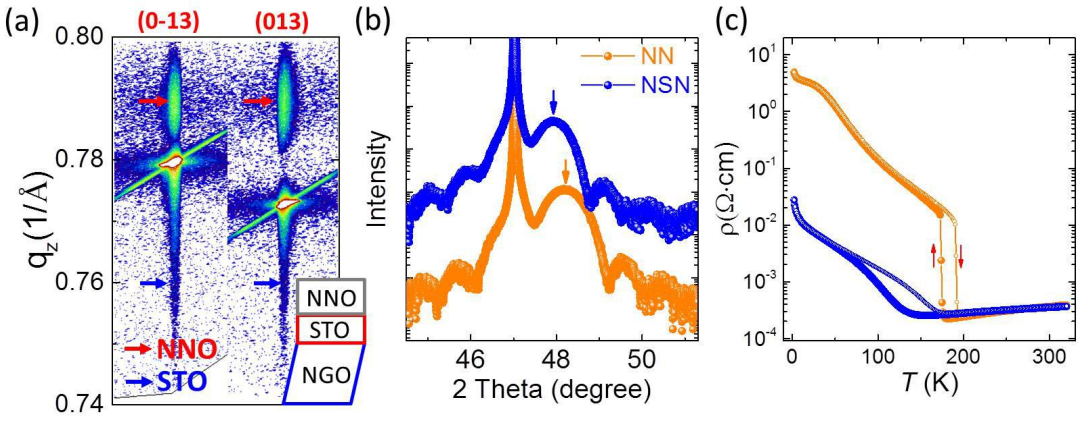

Figure 4: Manipulating the metal-to-insulator transition in $NdNiO_3$ film. (a) RSM of 6 uc STO buffered 30 uc NNO film on NGO substrate. (b) Theta-2Theta scan of a 30 uc NNO film on NGO without (NN) and with (NSN) a 6 uc STO buffer layer. The arrows indicate the peak position of NNO $(002)_{pc}$. (c) Temperature dependent resistivity of NNO films with and without STO buffer layer. The cooling and warming data are shown by big solid spheres and smaller open circles respectively.

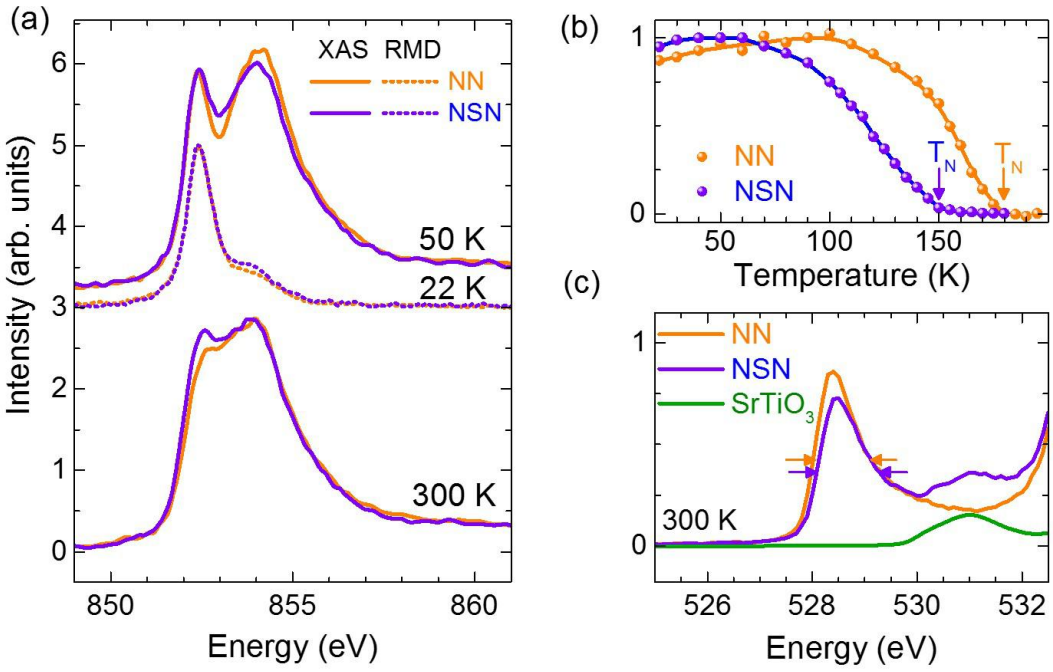

Figure 5: Symmetry tuned electronic structure and antiferromagnetic ordering in $NdNiO_3$ films. (a) Ni L_3-edge x-ray absorption (XAS) and resonant magnetic diffraction (RMD) for unbuffered (NN) and STO buffered (NSN) 30 uc NNO on NGO. (b) Temperature dependence of the magnetic diffraction intensity. The arrows indicate the Néel temperature, showing a decrease in the Néel temperature for the buffered film. (c) Oxygen K-edge spectra of the same samples at 300 K, showing an increased bandwidth for the buffered sample.